

SECONDARY MAXIMUM IN THE NEAR-INFRARED LIGHT CURVES OF TYPE Ia SUPERNOVAE

DANIEL KASEN¹

Received 2006 May 5; accepted 2006 June 2

ABSTRACT

We undertake a theoretical study of the near-infrared (NIR) light curves of Type Ia supernovae (SNe Ia). In these bands, the light curves are distinguished by a secondary maximum occurring roughly 20–30 days after the initial one. Using time-dependent multigroup radiative transfer calculations, we calculate the *UBVR_IJHK*-band light curves of model SN Ia ejecta structures. Our synthetic NIR light curves show distinct secondary maxima and provide favorable fits to observed SNe Ia. We offer a detailed explanation of the origin of the NIR secondary maximum, which is shown to relate directly to the ionization evolution of iron group elements in the ejecta. This understanding provides immediate insight into the dependence of the NIR light curves on the physical properties of the ejecta and in particular explains why brighter supernovae have a later and more prominent secondary maximum. We demonstrate the dependence of the NIR light curves on the mass of ⁵⁶Ni, the degree of ⁵⁶Ni mixing, the mass of electron capture elements, the progenitor metallicity, and the abundance of intermediate-mass elements (especially calcium). The secondary maximum is shown to be a valuable diagnostic of these important physical parameters. The models further confirm that SNe Ia should be excellent standard candles in the NIR, with a dispersion of $\lesssim 0.2$ mag even when the physical properties of the ejecta are varied widely. This study emphasizes the consummate value of NIR observations in probing the structure of SNe Ia and in furthering their cosmological utility.

Subject headings: radiative transfer — supernovae: general

Online material: color figures

1. INTRODUCTION

The extensive monitoring of Type Ia supernovae (SNe Ia) has typically focused on optical-band observations, with only occasional ventures into the infrared (Kirshner et al. 1973; Elias et al. 1981, 1985). The situation is now beginning to change, and near-infrared (NIR) observations over the 2 or 3 months following explosion are becoming more common, at least for the more nearby events. About a dozen SNe Ia have published, well-observed *JHK*-band light curves (e.g., Meikle 2000; Hernandez et al. 2000; Valentini et al. 2003; Candia et al. 2003; Krisciunas et al. 2001, 2003, 2004b, 2004c). NIR spectra have been obtained for several objects as well (Meikle et al. 1996; Bowers et al. 1997; Rudy et al. 2002; Höflich et al. 2002; Marion et al. 2003). Future SN Ia surveys promise to gather NIR light curves for a statistically interesting sample of events. With the broadening of our wavelength horizons comes the potential to probe the nature of SN Ia explosions in new ways.

Observational studies of SNe Ia in the NIR have often emphasized their cosmological utility (Krisciunas et al. 2004a). Normal SNe Ia are found to be excellent *standard* (as opposed to calibrated) candles in the NIR, with an intrinsic dispersion of less than 0.2 mag in the *J*, *H*, and *K* bands (Elias et al. 1985; Meikle 2000). Moreover, dust extinction is smaller by a factor ~ 5 in the NIR compared to the *V* band, largely eliminating uncertainties in the reddening corrections. The primary challenge for the cosmology studies, naturally, is that SNe Ia are much fainter and harder to observe in the NIR.

The NIR light curves of SNe Ia possess a morphology distinct from those at optical wavelengths. The *I*- through *K*-band light

curves are distinguished by the presence of a secondary maximum, occurring roughly 20–30 days after the initial one. A corresponding “shoulder” can often be seen also in the *R*- and *V*-band light curves. When the light from all bands is suitably integrated, the bolometric light curves sometimes show an inflection at these times as well (Contardo et al. 2000).

In the *I* band, the properties of the secondary maximum are found to correlate with the light-curve decline rate (and hence peak luminosity) of the supernova, being more prominent and occurring later in the broader/brighter SNe Ia (Hamuy et al. 1996b; Nobili et al. 2005). Very subluminal objects may lack a secondary maximum entirely. Similar trends appear in the *J*-, *H*-, and *K*-band light curves, although there are interesting exceptions to the rule (Krisciunas et al. 2001; Candia et al. 2003).

Occasional theoretical studies have touched on the NIR light curves of SNe Ia. Höflich et al. (1995) computed *I*-band and NIR light curves for several delayed-detonation models, many of which displayed secondary maxima. The authors explained the double-peaked behavior as a temperature-radius effect, in which the expansion of the photosphere compensates for the declining temperature in the ejecta. Wheeler et al. (1998) and Höflich et al. (2002) have further demonstrated the value of NIR spectra in diagnosing the physical conditions in the ejecta. Pinto & Eastman (2000) described the NIR secondary maximum as the release of preexisting trapped radiative energy due to a sudden decrease in the flux mean opacity. They placed special emphasis on the role played by stable iron group elements at the ejecta center in this process. Most significantly, Pinto & Eastman (2000) recognized the importance of the ionization state of the ejecta, in particular, the increased NIR emissivity of singly, as opposed to doubly, ionized iron group elements. This last idea is confirmed and extended in the models studied here.

Despite the theoretical insights, the origin of the NIR secondary maximum and its dependence on the SN ejecta properties have remained in many ways, and to many people, obscure. Moreover,

¹ Allan C. Davis Fellow, Department of Physics and Astronomy, Johns Hopkins University, 3400 North Charles Street, Baltimore, MD 21218, and Space Telescope Science Institute, 3700 San Martin Drive, Baltimore, MD 21218; kasen@pha.jhu.edu.

theoretical models of SNe Ia have often had difficulty in fitting the distinctive double-peaked *I*-band light curves (e.g., Höflich & Khokhlov 1996; Pinto & Eastman 2000; Blinnikov & Sorokina 2004), whereas very few NIR light-curve calculations have been attempted (cf. Höflich et al. 1995). This paper focuses exclusively on theoretical models of the far-red and NIR light curves of SNe Ia. We calculate the synthetic light curves of parameterized ejecta configuration using the time-dependent multidimensional radiative transfer code SEDONA (§ 3). Our model light curves show distinct secondary maxima and provide reasonable fits to the observed *R*-, *I*-, *J*-, and (to a lesser extent) *H*- and *K*-band light curves of SNe Ia (§ 4).

Close examination of our model calculations provides a clear-cut explanation for the NIR secondary maximum in SNe Ia (§ 5). The double-peaked behavior is directly related to the ionization evolution of iron group elements in the SN ejecta. In particular, the NIR emissivity of iron/cobalt increases sharply at a temperature $T \approx 7000$ K, marking the transition between the singly and doubly ionized states. The eventual cooling of the iron-rich layers of ejecta to this temperature is thus accompanied by a sudden increase in emission at far-red and NIR wavelengths.

Understanding the origin of the secondary maximum provides immediate insight into the dependence of the NIR light curves on the ejecta properties and allows for theoretical explanations of the empirically established correlations (§ 6). In particular, we study the effect of variations in the mass of ^{56}Ni , the degree of mixing of ^{56}Ni , the mass of electron capture elements, the progenitor metallicity, and the abundance of intermediate-mass elements (IMEs; especially calcium). All effects are confirmed with illustrative theoretical models. The NIR secondary maximum is shown to be a valuable diagnostic of these important physical parameters. The models further demonstrate that SNe Ia are indeed excellent standard candles in the NIR, even when the physical properties of the ejecta are varied widely (§ 7).

2. THE NEAR-IR EMISSION OF SNe Ia

Before turning to the light-curve models, we consider the source of NIR emission in SN Ia atmospheres. The luminosity of a SN Ia is powered entirely by the decay of radioactive isotopes synthesized in the explosion, in particular, ^{56}Ni in the decay chain $^{56}\text{Ni} \rightarrow ^{56}\text{Co} \rightarrow ^{56}\text{Fe}$. The energetic products of the decay (primarily gamma rays) heat the SN ejecta, which radiate thermally. The bulk of the radiation occurs initially at ultraviolet (UV) and blue wavelengths. Direct emission at NIR wavelengths (from bound-free and free-free sources) is typically of minor significance.

A portion of the blue/UV radiation pervading the SN ejecta is degraded to red and NIR wavelengths by interaction with lines. The primary redistribution mechanism is fluorescence (Höflich 1995; Pinto & Eastman 2000), whereby a UV photon excites a high-energy atomic transition, then de-excites via a cascade of longer wavelength transitions (the reverse process is also possible and occurs as well; Mazzali & Lucy 1993). The wavelength redistribution of radiation in atomic lines is responsible for virtually all of the NIR emission observed from SNe Ia. The high velocity gradient in the ejecta Doppler-broadens the radiation from each individual transition, and the radiation from literally millions of lines blurs together to form a pseudocontinuum emission in the NIR.

We can calculate, in an approximate way, the NIR opacity and emissivity due to the large complex of lines. A convenient way to capture the average effect is through an expansion opacity formalism (Karp et al. 1977; Eastman & Pinto 1993), in which

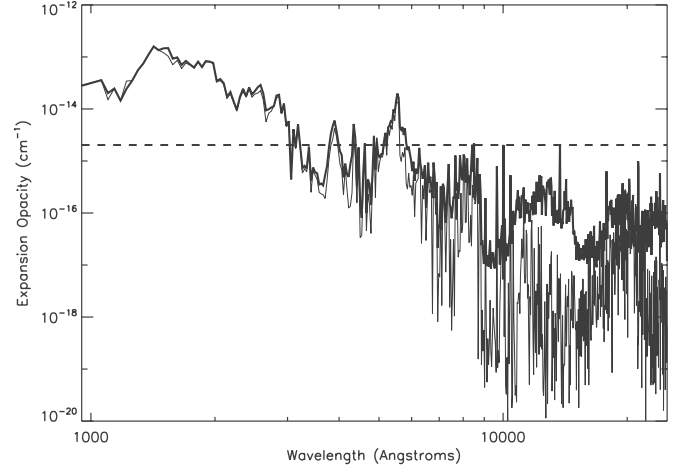


FIG. 1.—Opacity as a function of wavelength of a parcel of cobalt/iron-rich ejecta gas at density $\rho = 10^{-14} \text{ cm}^{-3}$, temperature $T = 15,000$ K, and time since explosion $t_{\text{exp}} = 20$ days. The composition is 75% ^{56}Co , 24% iron, and 1% ^{56}Ni . LTE level populations are assumed. The thick line shows the bound-bound expansion opacity (eq. [1]) calculated using the Kurucz CD1 atomic line list (~42 million lines), while the thin line is that calculated using the Kurucz CD1 line list (~500,000 lines). Note the large differences in the near-IR. The horizontal dashed line marks the electron-scattering opacity level. [See the electronic edition of the *Journal* for a color version of this figure.]

individual lines are summed together to form a pseudocontinuum opacity

$$\alpha_{\text{exp}}(\lambda) = \frac{1}{ct_{\text{exp}}} \frac{\lambda}{\Delta\lambda} \sum_i (1 - e^{-\tau_i}), \quad (1)$$

where t_{exp} is the time since explosion. The sum runs over all lines in the wavelength bin of size $\Delta\lambda$ at wavelength λ . The quantity τ_i is the Sobolev line optical depth (Mihalas 1978).

In Figure 1, we show the expansion opacity calculated for a parcel of iron/cobalt-rich ejecta gas at density $\rho = 10^{-13} \text{ cm}^{-3}$, temperature $T = 15,000$ K, and time $t_{\text{exp}} = 20$ days, typical of the inner layers of SNe Ia. We use the Kurucz CD1 atomic line list containing ~42 million lines and compute the atomic level populations, assuming local thermodynamic equilibrium (LTE). The iron group expansion opacity increases sharply toward the blue, due to the much larger number of iron group lines occurring at shorter wavelengths.

In Figure 1, we also compare the expansion opacity computed using the much smaller (but commonly applied) Kurucz CD 23 line list, containing only ~500,000 lines. Although the two lists give similar results in the blue, order-of-magnitude differences appear in the NIR. This emphasizes the large number (~5 million) of relatively weak lines that may contribute to the NIR emission of SNe Ia.

Assuming LTE, the monochromatic emissivity η_λ is given by the opacity α_{exp} times the blackbody function $B_\lambda(T)$. Because we are ultimately interested in the total NIR emission over a broadband wavelength region, we define an average emissivity per gram (units $\text{ergs s}^{-1} \text{ g}^{-1} \text{ Å}^{-1}$) over the broadband filter F by convolving the monochromatic emissivity with the appropriate filter transmission function $\phi_F(\lambda)$

$$\bar{\eta}_F(T) = \frac{1}{\rho} \frac{\int_0^\infty d\lambda \phi_F(\lambda) B_\lambda(T) \alpha_{\text{exp}}(T, \lambda)}{\int_0^\infty d\lambda \phi_F(\lambda)}. \quad (2)$$

Although this expression formally represents a thermal emission source, under certain conditions it also approximates the operative

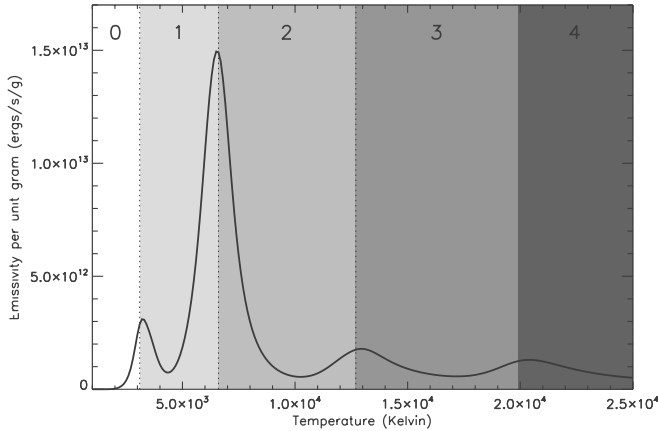


FIG. 2.—Mean I -band emissivity (as a function of temperature) for the iron/cobalt gas discussed in Fig. 1 at density $\rho = 10^{-14} \text{ cm}^{-3}$ and time since explosion $t_{\text{exp}} = 40$ days. Calculations use eq. (2), the Kurucz CD1 atomic line list, and the Bessell (1990) I -band filter profile. The shading illustrates the ionization fraction of the gas, which changes very sharply with temperature at the edges marked in the figure. A strong peak in emissivity is seen at the transition between the singly and doubly ionized states ($2 \rightarrow 1$) occurring at $T \approx 7000$ K.

line fluorescence process well. In the limit that the timescales for radiative transitions are short compared with other timescales of interest, the radiation field in the lines approaches the thermodynamic limit embodied by the Planck function. These are the conditions that drive the line source function and level populations close to that of LTE and should hold approximately at least for the complex iron group species in the deeper layers of ejecta (Baron et al. 1996). Given the dominance of the radiative rates, the temperature T appearing in equation (2) should be considered more representative of the radiation field, rather than the electron gas. However, the weak coupling through bound-free and free-free processes may bring the gas and radiation into equilibrium as well (Pinto & Eastman 2000).

Note that, even assuming LTE, the wavelength dependence of the emissivity is not a smooth blackbody function, but depends on the number of lines with substantial opacity in a given part of the spectrum. As a result, the NIR emissivity shows a very interesting nonlinear dependence on temperature. In Figure 2, we see that the mean I -band emissivity ($\bar{\eta}_I$) of iron/cobalt-rich gas peaks sharply at temperatures at which the gas is near an ionization edge. The most prominent peak is at temperature $T_{21} \approx 7000$ K, marking the transition between the singly and doubly ionized states (hereafter termed the $2 \rightarrow 1$ ionization edge or front).

The interesting dependence of the NIR emissivity on temperature has a simple explanation in terms of the atomic physics. NIR radiation arises from transitions between relatively closely spaced atomic energy levels. The atomic levels are generally more closely spaced at high excitation energy (i.e., high atomic number n). Thus, for a given ionization state, the NIR emission increases with temperature as the excited levels become increasingly populated. When the temperature becomes hot enough to ionize the species, however, the NIR emissivity drops rapidly. The ionized species has a higher overall energy scale (being more tightly bound), and hence its excited levels are not highly populated. If the temperature is increased further, this behavior is repeated until the next ionization stage is reached. We emphasize that this emissivity dependence has nothing to do with the energy released from recombination itself, which makes a negligible contribution to the overall energy budget.

For completeness, Figure 3 shows the emissivity for several wavelength bands and for compositions of pure iron, pure cobalt,

and a mixture of silicon and sulfur. The emissivity of the iron group species is qualitatively similar in all NIR bands. A peak at $T_{21} = 7000$ K occurs also in the optical B and V bands, although it is much less prominent than in the NIR. The relative size of the emissivity peaks depends on the details of atomic structure and thus varies somewhat between iron and cobalt and in the different wavelength regions. In general, the iron group emissivity exceeds that of IMEs such as silicon and sulfur, except at very high temperatures. This is because the complex iron group valence electron structure leads to an extremely large number of line transitions.

The emissivity behavior shown in Figure 2 turns out to be the key to understanding the NIR secondary maximum in SNe Ia. When the iron-rich layers of SN ejecta begin cooling to $T_{21} \approx 7000$ (which occurs roughly 35–40 days after the explosion), the gas becomes very effective in redistributing the blue/UV radiation to longer wavelengths. This leads to the rebrightening of the NIR light curves. During these phases, one expects the NIR emission to be dominated by the relatively thin shell of material located near the ionization front at T_{21} . As the ejecta progressively cools, this shell recedes deeper into the ejecta, following the inward propagation of the $2 \rightarrow 1$ recombination.

The secondary maximum in the NIR light curves is thus identified with the onset and recession of the $2 \rightarrow 1$ ionization front into iron-rich ejecta. In the next few sections we delineate the process in detail, and show how it serves as an interesting probe of the SN ejecta structure.

3. THEORETICAL SNe Ia LIGHT-CURVE MODELS

A short time (~ 1 minute) after the explosion of a SN Ia, hydrodynamic and nucleosynthetic processes abate, and the ejected material reaches a phase of nearly free expansion. Thereafter, the essential theoretical challenge becomes simulating the production and diffusion of photons through the hot and optically thick ejecta, i.e., the radiative transfer problem. Here we calculate broadband model light curves by solving the transfer equation using the multidimensional time-dependent Monte Carlo code SEDONA (Kasen et al. 2006).

3.1. Model Ejecta Structures

To demonstrate the basic dependencies of the NIR light curves, we calculate synthetic SEDONA light curves for simple, hand-constructed SN Ia ejecta models. In the free-expansion phase, the velocity of the ejecta is homologous and everywhere proportional to the radius, $r = vt_{\text{exp}}$, where t_{exp} is the time since explosion. Given the self-similar nature of the flow, velocity is used as the spatial coordinate in the simulation.

Polarization observations of SNe Ia demonstrate that the asymmetry of the ejecta is typically not large (Wang et al. 2003). We therefore only consider spherically symmetric ejecta structures in this paper. Deviations from sphericity do not influence the basic radiative transfer effects identified here, although they lead to some dependence of the model light curves on orientation.

In one-dimensional (1D) hydrodynamic explosion models of SNe Ia, such as W7 (Nomoto et al. 1984), the final ejecta density structure is well characterized by an exponential. We therefore take the density profile of our ejecta models to be

$$\rho(v, t) = \frac{M_{\text{Ch}}}{8\pi v_e^3 t^3} \exp(-v/v_e), \quad (3)$$

where M_{Ch} is the Chandrasekhar mass and the velocity scale $v_e = 2750 \text{ km s}^{-1}$ is determined by setting the kinetic energy $\text{KE} = 6M_{\text{Ch}}v_e^2$ equal to the energy released in burning $1.25 M_{\odot}$ of the original carbon/oxygen white dwarf (1.6×10^{51} ergs).

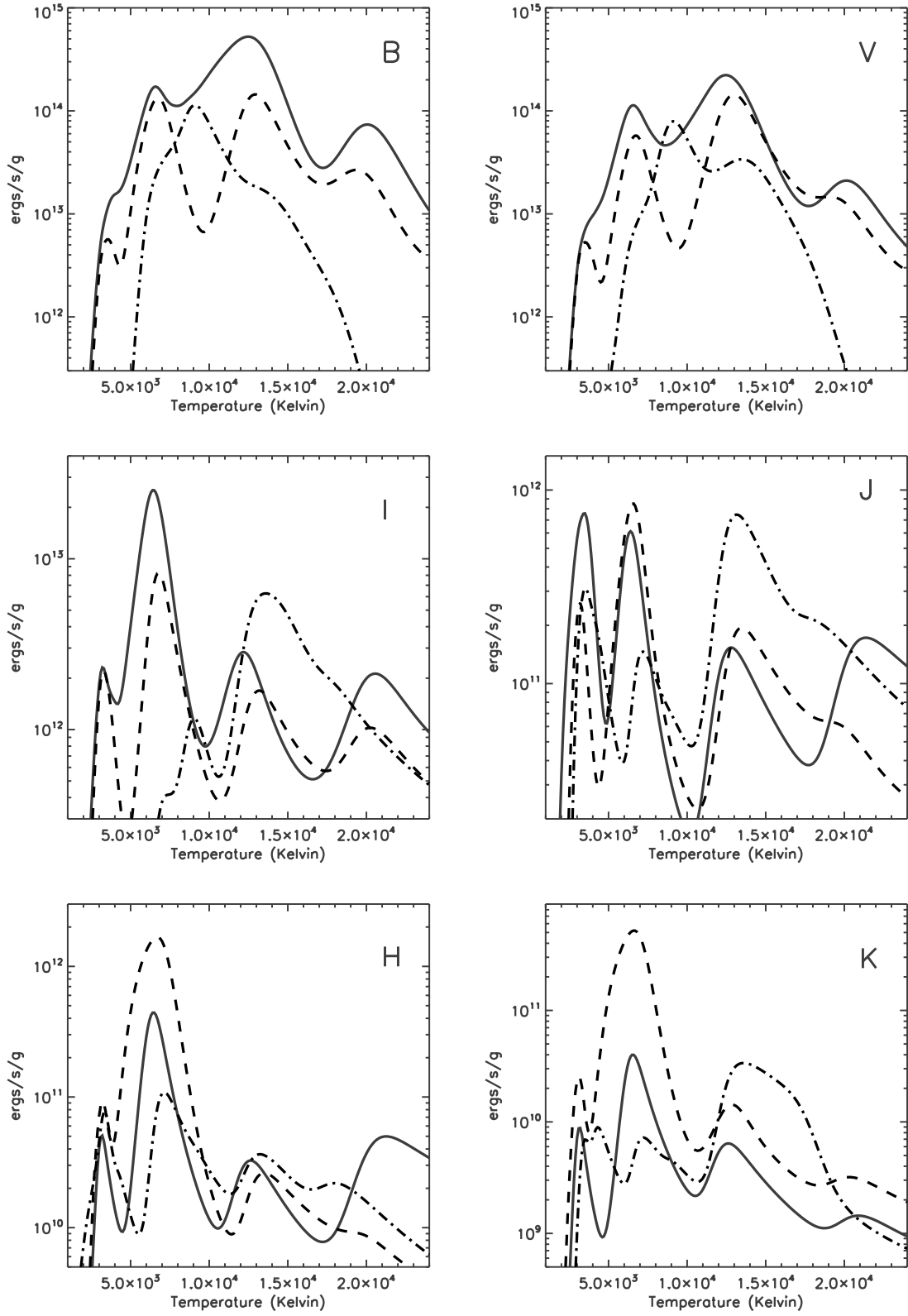


FIG. 3.—More complete plot of the mean NIR emissivity demonstrated in Fig. 2, this time shown for each of the *BVLJHK* bands and for three compositions: pure iron (*solid line*), pure cobalt (*dashed line*), and a mix of 70% silicon and 30% sulfur (*dot-dashed line*). The density is $\rho = 10^{-14} \text{ cm}^{-3}$, and the time since explosion $t_{\text{exp}} = 40$ days. [See the electronic edition of the *Journal* for a color version of this figure.]

In analogy to well-known 1D explosion models such as W7, we tailor a four-zone stratified compositional structure. For our fiducial model these zones, from the center out, are (1) $0.05 M_{\odot}$ of stable iron-peak elements (specifically ^{54}Fe and ^{58}Ni , typical of electron capture); (2) $0.6 M_{\odot}$ of radioactive ^{56}Ni ; (3) $0.6 M_{\odot}$ of IMEs, specifically, Si, S, Ar, and Ca, in proportion to their solar abundances; and (4) $0.15 M_{\odot}$ of unburned carbon-oxygen with solar metallicity.

To smoothly connect these zones, we use a Gaussian function that allows us to control the degree of mixing. For example, mixing between the ^{56}Ni and IME layers is assumed to occur over a mass range defined by the free parameter a_{Ni} . Above the interface between the two zones (mass coordinate $m_n = M_{\text{Fe}} + M_{\text{Ni}} - a_{\text{Ni}}/2$) the nickel abundance is taken to fall off as

$$X_{\text{Ni}} = \exp[-(M - m_n)^2/a_{\text{Ni}}^2], \quad (4)$$

while the IME abundance is $X_{\text{IME}} = 1 - X_{\text{Ni}}$. Similar mixing parameters are defined for the iron and ^{56}Ni interface (a_{Fe}) and the IME and unburned interface (a_{IME}). In our fiducial model we use $a_{\text{Ni}} = 0.1$, $a_{\text{Fe}} = 0.05$, and $a_{\text{IME}} = 0.1$. In fact, only a_{Ni} is of real consequence to the NIR light curves (§ 6.1).

The rough compositional structure described, while only suggestive of detailed explosion models, is quite adequate for our purposes. The NIR light curves are not sensitive to the detailed trace abundances, with one important exception, as we discuss in § 6.4; small amounts of calcium can affect the *I* band, due to the overwhelming strength of the Ca II IR triplet feature. In all other bands, the overriding factor is the amount and distribution of iron group elements.

3.2. Technical Considerations of the Radiative Transfer

Given a homologously expanding SN ejecta structure, the time-dependent SEDONA code calculates high-resolution synthetic spectra at each day, from day 1 to several months after the explosion. Broadband light curves are then constructed by convolving the spectrum at each time with the appropriate filter transmission functions. We use the filter profiles of Bessell (1990) for the optical bands and those of Persson et al. (1998) for the *JHK* bands.

SEDONA includes a detailed treatment of gamma-ray transfer to determine the instantaneous energy deposition rate from radioactive ^{56}Ni and ^{56}Co decay. Radiative heating and cooling rates are evaluated from Monte Carlo estimators, and the temperature structure of the ejecta is determined by iterating the model to thermal equilibrium. The present calculations use 120 radial zones, 100 time points, and 5000 wavelength groups. Resolution tests confirm the adequacy of this gridding for the problem at hand.

Several significant approximations are made in SEDONA, notably the employment of LTE level populations and ionization. In addition, bound-bound line transitions are treated using the expansion opacity formalism (eq. [1]) and an approximate two-level atom approach to wavelength redistribution. The ratio of absorption to scattering in lines is calibrated from detailed atomic models and is always close to 1. Special care, however, is taken for the calcium lines, which are assumed to be pure scattering, for the reasons discussed in § 6.4. Note that SEDONA allows for a direct Monte Carlo treatment of line fluorescence, but due to computational constraints this functionality is not exploited here. See Kasen et al. (2006) for further code description and verification.

In the tenuous atmospheres of SNe Ia, the microscopic conditions assuring the establishment of LTE level populations and

ionization (namely, the dominance of collisional rates) are in fact not met. A direct treatment of the non-LTE physics is thus highly desirable. Unfortunately, a solution of the non-LTE rate equations, including the ≥ 5 million potentially important line transitions, challenges the computational capacity of even the most advanced time-independent spectrum codes. In a fully time-dependent light-curve calculation, the adoption of LTE at some level appears inevitable. Fortunately, a wide range of theoretical calculations confirm the adequacy of LTE in reproducing the essential spectral and photometric properties of SN Ia models in both the optical and NIR (e.g., Höflich et al. 1995; Baron et al. 1996; Pinto & Eastman 2000; Wheeler et al. 1998). In particular, the crucial iron group species responsible for continuum formation have extremely complex atomic structures and numerous closely spaced atomic levels and may therefore roughly approximate their equilibrium distributions. However, in other atomic species responsible for individual strong line features non-LTE effects may be significant (especially calcium; see § 6.4). In addition, because the ionization state of the ejecta is of particular importance to the NIR light curves, LTE becomes increasingly suspect at later times ($t_{\text{exp}} \gtrsim 70$ days), when the nonthermal ionization by radioactive gamma rays becomes significant (§ 4).

An additional, perhaps more serious issue for the transfer calculations, is the (in)adequacy of the available atomic data. Because NIR emission occurs in millions of relatively weak atomic lines, using a complete and accurate atomic line list is critical. We have found the commonly applied CD 23 line list of Kurucz (1993; which contains nearly 500,000 lines) to be insufficient for calculating the *IJK*-band light curves. Upgrading to the Kurucz CD 1 line list (with ~ 42 million lines) affords significant improvement; however, even this list is likely incomplete and/or inaccurate to some degree. The inadequacy of the line data at long wavelengths likely plagues our synthetic NIR light curves, as we discuss further in § 4.

4. MODEL NIR LIGHT CURVE OF A NORMAL SN Ia

We have calculated the full spectral evolution and broadband light curves for our fiducial SN Ia model containing $0.6 M_{\odot}$ of ^{56}Ni . Figure 4 compares the model optical and NIR light curves to observations of SN 2001el, a photometrically normal SN Ia with extensive coverage obtained by Krisciunas et al. (2003). The observed light curves have been corrected for dust extinction using the estimates $A_v = 0.57$ (Krisciunas et al. 2003) and $R_v = 2.88$ (Wang et al. 2003). We select a distance modulus to SN 2001el of $\mu = 31.4$ in order to align the peak of the observed *V*-band light curve with that of the model. This improves the visual comparison of the light-curve shapes. In fact, Krisciunas et al. (2003) estimate a slightly smaller distance of 31.29 ± 0.08 using the width-luminosity relation of Phillips et al. (1999). This suggests that our synthetic light curves are perhaps ~ 0.1 mag brighter than the observed and that a model with slightly lower M_{Ni} (e.g., $0.55 M_{\odot}$) may be more appropriate for SN 2001el.

The characteristic double-peaked morphology is clearly apparent in all our model NIR light curves, with a distinct and prominent secondary maximum occurring in the *I*, *J*, *H*, and *K* bands. A corresponding “shoulder” is also seen in the *R* band and in the bolometric light curve as well (Fig. 8). On the whole, the model *V*-, *R*-, *I*-, and *J*-band light curves do a favorable job of fitting those of SN 2001el, at least for epochs $t_{\text{exp}} < 60$ days. The models become less accurate at later times, but this is also when the transfer calculations are expected to be less reliable. In the model *I*-band light curve, the decline from the first maximum is somewhat too rapid, and the secondary maximum occurs slightly earlier than in the observations. We note that the prominence and timing of

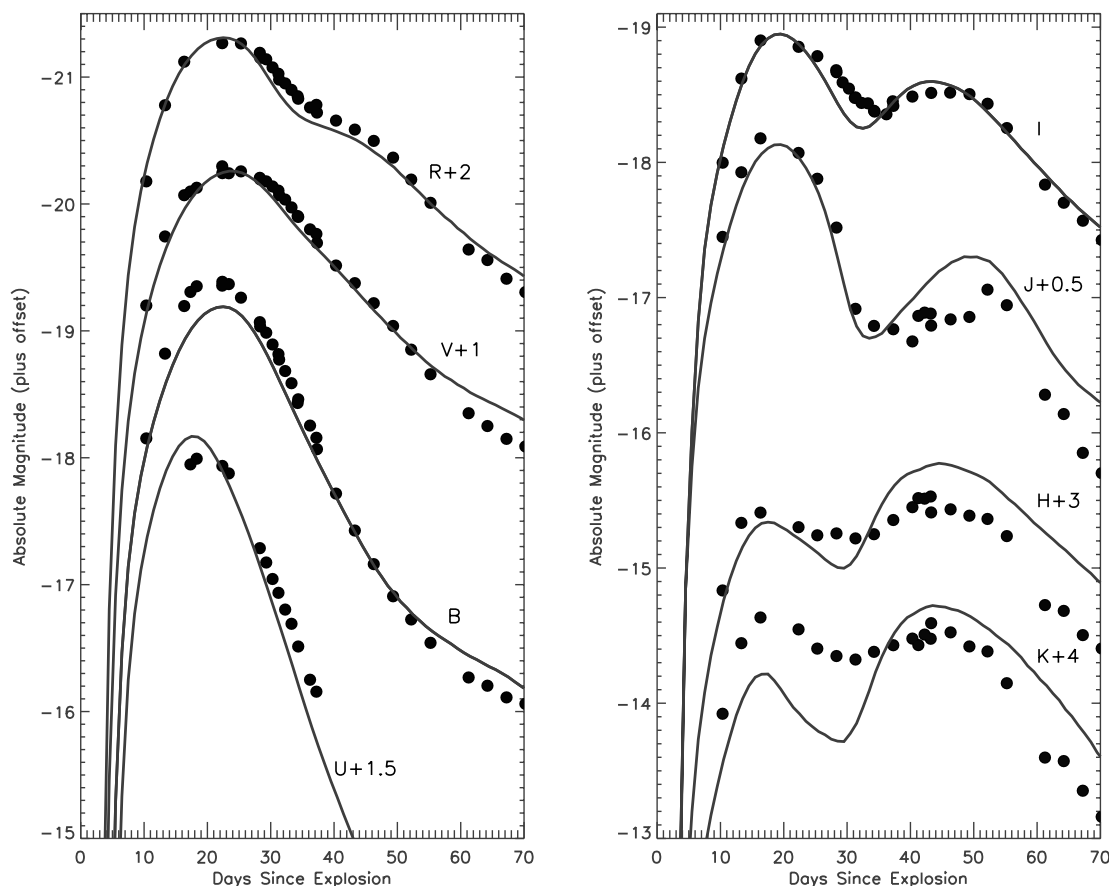


FIG. 4.—Broadband light curves of the fiducial model (curves) compared to observations of SN 2001el (circles). [See the electronic edition of the *Journal* for a color version of this figure.]

the secondary maximum is quite sensitive to the model parameters (see § 6) and also shows wide variation in the observations (Nobili et al. 2005). A thorough exploration of the model parameter space would likely yield an improved fit to SN 2001el, perhaps in the process illuminating its particular physical characteristics. In addition, polarization observations of SN 2001el indicate that the ejecta was not perfectly spherically symmetric (Wang et al. 2003; Kasen et al. 2003); therefore, aspherical ejecta structures may need to be considered to exactly account for all of the light-curve properties.

The model does a poorer job in the *H* and *K* bands. In the observations the *H*- and *K*-band light curves are relatively flat for roughly 20 days after *B*-band maximum ($t_{\text{exp}} = 18$ days), whereas the models, in contrast, show a strong rise to the secondary maximum during these phases. This is because the model underestimates the luminosity of the initial maximum relative to the secondary one. Attempts to improve the *H* and *K* fits by varying the model ejecta structure proved unsuccessful.

It is possible that the relatively poor *H*- and *K*-band light-curve fits relate to an inadequacy of the LTE approximation or signal a missing ingredient in our model ejecta structures. However, the primary reason is likely the inadequacy of the atomic line list. We demonstrate the importance of the atomic data by recomputing the light curves using the restricted line list Kurucz CD23 (containing only 500,000 lines) and comparing to those of our standard line list (Kurucz CD1, with 42 million lines). The differences in the *IJHK* light curves are considerable (Fig. 5), especially at early times. This is not surprising, given the large differences noticed in the opacity calculations of Figure 1.

On the whole, the CD23 *IJHK* light curves do a dramatically poorer job of fitting the observations. In particular, the initial maximum is much too weak in all bands. The problem can be traced directly to the relative lack of higher ionization, longer wavelength iron group lines in the CD23 list. The use of an inadequate line list may be one reason why previous theoretical models have sometimes had difficulty fitting the *I*-band light curves of SNe Ia. Although CD1 offers significant improvement over CD23, it is natural to suspect that, were an even more extensive line list available, our model *H*- and *K*-band light curves might show significant improvement.

Although not the focus of this paper, we also present NIR spectra of the fiducial model at a few different epochs in Figure 6. Near maximum light, the NIR spectrum is quite featureless, with the occurrence of only a few weak line features from IMEs. At later times, prominent emission features from blended iron group lines arise near 1.6 and 1.8 μm . The spectra in Figure 6 show the same general features identified in the model calculations of Wheeler et al. (1998). The reader can look there for a detailed spectroscopic analysis and comparison with observations.

5. EXPLANATION OF THE SECONDARY MAXIMUM

In our models, we trace the origin of the secondary maximum directly to the ionization evolution of iron group elements in the ejecta. In particular, as discussed in § 2, the NIR emissivity increases sharply at temperature $T_{21} \approx 7000$ K in iron/cobalt gas, marking the transition between the doubly and singly ionized states (i.e., the $2 \rightarrow 1$ ionization edge; see Fig. 2). For reasons already discussed, the iron-rich gas becomes exceptionally *phosphorescent*

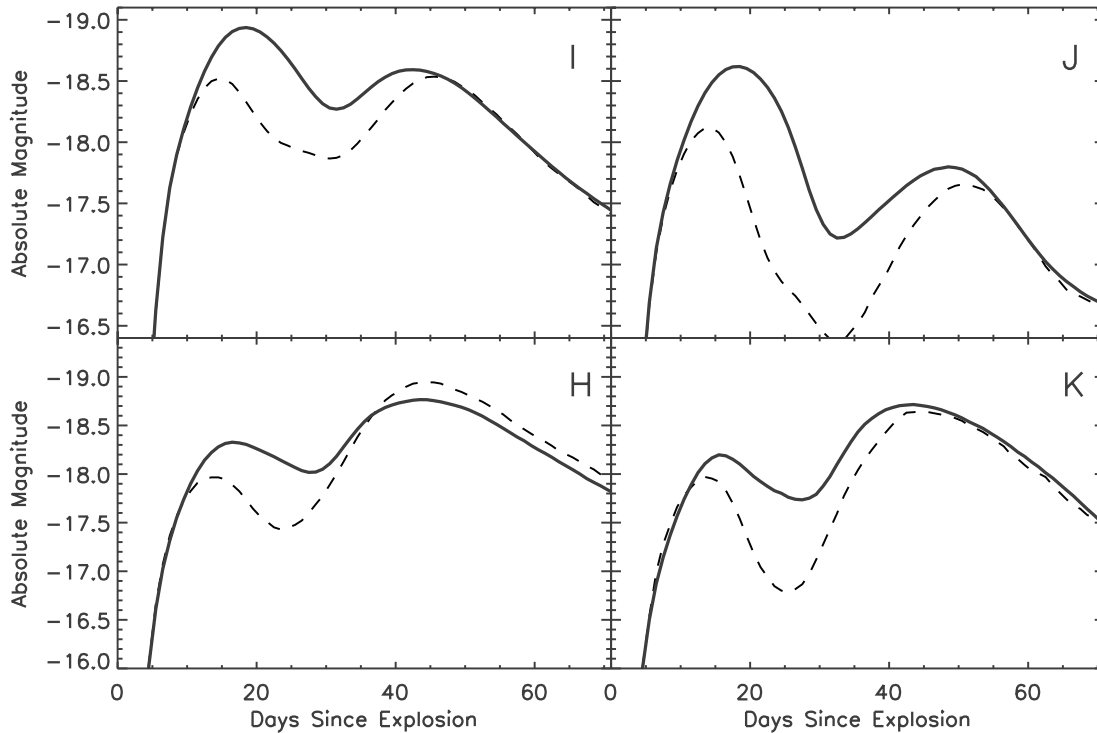


FIG. 5.—Comparison of the *IJHK* light curves of the fiducial model calculated using two different atomic line lists, the 500,000 line Kurucz CD 23 (*dashed lines*) and the 42 million line Kurucz CD 1 (*solid lines*). Due to the lesser number of lines, the first maximum of the CD23 light curves is depressed relative to CD1 in all bands. [See the electronic edition of the *Journal* for a color version of this figure.]

at this temperature and is very effective in redistributing the pervading UV/blue radiation to longer wavelengths.

Because the temperature in the ejecta decreases with radius, the region near the $2 \rightarrow 1$ ionization front comprises a relative thin shell of material. During the hot, early epochs, this region lies in the far outer layers of ejecta, but as the SN cools, overall the ionization front recedes deeper (in a Lagrangian sense) into the ejecta. The resulting inward propagating “recombination wave” resembles that often described in models of hydrogen-rich Type IIP SNe. However, in contrast to the SNe IIP, the flux mean opacity in SNe Ia does not change substantially over the ionization front, and the temperature gradient remains gradual. It is the onset of this recombination wave into the iron-rich core of ejecta that leads to a sudden increase in NIR emission and the rebrightening of the SN in a secondary maximum.

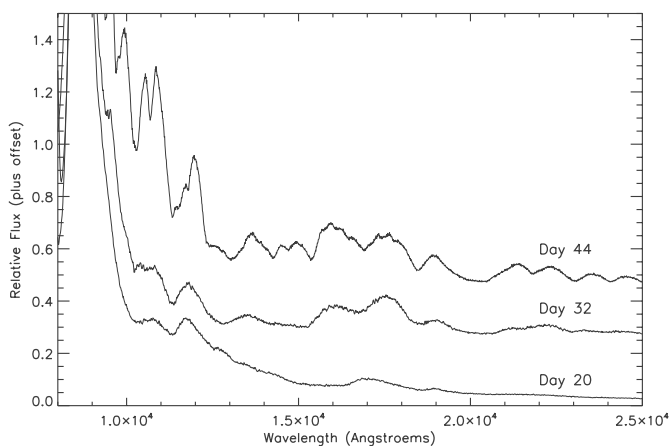


FIG. 6.—Near-infrared spectra of the fiducial SN Ia model at three different epochs. Labels indicate time since explosion.

To delineate this process in detail, we examine the evolution of the NIR emission over time. Like the frames of a comic strip, the panels in Figure 7 depict successive chronological states of the spatial distribution of NIR emissivity (in this case, *J* band) for the fiducial SN Ia model discussed in § 4. Each panel shows the radial contribution to the *J*-band emission at a given time, specifically $d\psi(r) = \eta_J(r)r^2 dr$, where r is the radius and η_J is the broadband emissivity calculated using equation (2). This figure is meant mainly as a heuristic; the observed luminosity in the optically thick phases depends not only on the instantaneous emission, but also on the transfer of radiation through the ejecta.

Given the self-similar nature of the flow, velocity is used as the radial coordinate in Figure 7. The red hatched region identifies the iron-rich core, which extends to roughly 7000 km s^{-1} in the model. The green shaded region marks the region near the $2 \rightarrow 1$ ionization front (specifically, the ionization fraction between 1.5 and 1.9). The width of this region, which depends on the temperature gradient, is typically a few thousand km s^{-1} . With time, the ejecta cool, and the green shaded region can be seen moving inward, marking the propagation of the $2 \rightarrow 1$ recombination wave.

We offer a step-by-step discussion of Figure 7. During the early epochs (day 15 after explosion), most of the *J*-band emission comes from throughout the hot iron core, which has an ionization fraction between 3 and 4. Note that the emission is always greatest near the ionization fronts, which are conspicuous as the emission peaks in the figure. At these early times, the ejecta is optically thick at NIR wavelengths to both electron scattering and bound-bound expansion opacity. The rise time to the first *J*-band maximum at $t_{\text{exp}} = 19$ days is thus related to the diffusion time of photons (Arnett 1982).

Following the first *J*-band maximum, the hot iron core is in the process of recombining from triply to doubly ionized. At these times (days 20 and 25) the NIR emission is dominated by the

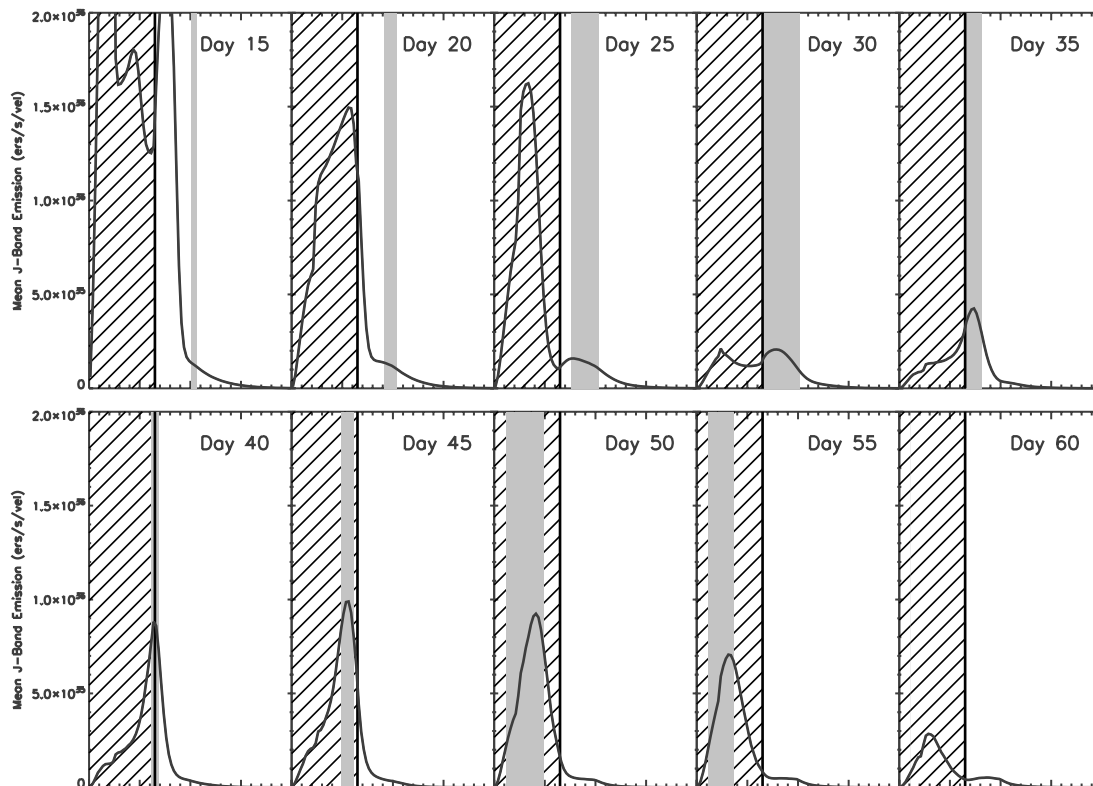


FIG. 7.—Comic strip explaining the origin of the secondary maximum in the NIR light curves of SNe Ia. The figure shows the time evolution of the radial distribution of the instantaneous mean J -band emission (solid lines). For each panel, the ejecta velocity coordinate is shown on the x -axis, ranging from zero to 20,000 km s^{-1} . The hatched region marks the iron core, which extends to $v = 7000 \text{ km s}^{-1}$. The shaded region marks the region near the $2 \rightarrow 1$ ionization front. A large spike in J -band emission occurs when that front reaches the iron-rich layers of the ejecta, leading to the NIR secondary maximum. [See the electronic edition of the *Journal* for a color version of this figure.]

rather thin shell of material near the $3 \rightarrow 2$ ionization front. Meanwhile, the $2 \rightarrow 1$ ionization front forms well outside the iron core and contributes little NIR emission.

By day 30 after explosion the iron core has nearly completely recombined to doubly ionized and, with the passing of the $3 \rightarrow 2$ ionization front, the NIR emissivity has decreased significantly. This is the local minimum in the J -band light curve. The light curve would continue to decrease monotonically if it were not for the impending onset of the $2 \rightarrow 1$ recombination wave. Already this wave has reached the layers just above the iron core, where a small emission peak is visible.

At day 35 the recombination wave reaches the edge of the iron core, and the NIR emission begins to increase dramatically. This is exactly the time at which the model J -band light curve begins to rebrighten. The NIR emission is now dominated by the “fluorescent shell” at the $2 \rightarrow 1$ ionization front. The ejecta are largely transparent in the NIR, and radiation emitted from the shell escapes almost immediately. Over the next 2 weeks, the fluorescent shell recedes further into the iron core, until, at day 50, it is completely contained in the iron-rich region. This marks the peak of the J -band secondary maximum.

At later times, as the fluorescent shell recedes yet deeper in the ejecta, its volume decreases, and so does the J -band brightness. By day 60, the $2 \rightarrow 1$ recombination wave has completely passed, and the iron core is nearly entirely singly ionized. The NIR emission is low and continues to decline.

Why is a secondary maximum seen strongly in the NIR, but not in the optical light curves? During the epochs of the secondary maximum, the ejecta remain optically thick at bluer wavelengths ($\lambda \lesssim 5000 \text{ \AA}$). The onset of the $2 \rightarrow 1$ recombination of iron group

elements further increases the opacity in the optical due to the development of broad blends of Fe II and Co II lines in the B and V bands. Thus, optical radiation at the $2 \rightarrow 1$ ionization front cannot immediately escape the ejecta, but continues to diffuse out gradually or to fluoresce to longer wavelengths. Meanwhile, the ejecta are transparent in the NIR, and photons fluorescing to these wavelengths escape straightaway. The net effect of the recombination wave is therefore to redistribute flux from the optical to longer wavelengths.

In Figure 8, we see that at the onset of the secondary maximum (day 35 after explosion) a slight bump also occurs in the model bolometric light curve. This inflection has been noted in observed SN Ia light curves (Contardo et al. 2000) and has been explained by Pinto & Eastman (2000) as the release of preexisting trapped radiative energy. The ejecta are optically thick (at bluer wavelengths) for the first couple months after explosion, and the average diffusion time of photons is a significant fraction of the expansion time. A store of trapped radiation continually accumulates in the supernova ejecta. It is the gradual leaking of this energy reservoir that causes the bolometric luminosity to exceed the instantaneous radioactive energy deposition rate from day 18 until full transparency is reached near day 70. At day 35 the onset of the $2 \rightarrow 1$ ionization front in the iron core suddenly enhances photon escape via fluorescence into the NIR. This opens up a new means of release of the trapped SN radiation, causing a slight rise in the bolometric light curve.

As an interesting aside, note that the NIR emissivity also peaks when the gas recombines from singly ionized to neutral (Fig. 2). In principle, the propagation of another recombination wave ($1 \rightarrow 0$), could lead to a *third* bump in the NIR light curves.

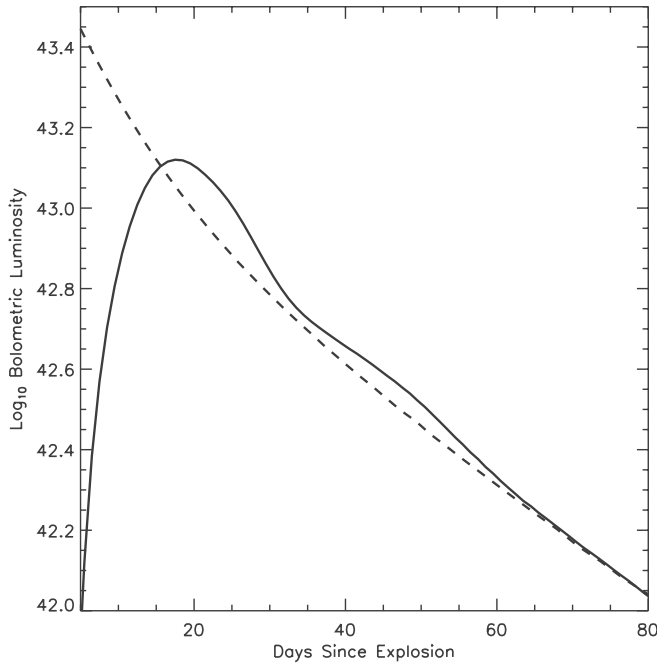


FIG. 8.—Bolometric light curve (solid line) and radioactive energy deposition rate (dashed line) for the fiducial model. An inflection in the bolometric light curve (corresponding to the NIR secondary maximum) is seen beginning at day 35 after explosion.

In the current models, a third maximum is in fact seen at $t_{\text{exp}} \approx 100$ days (~ 80 days after B -band maximum), most prominently in the J band. However, the inadequacies of the LTE approximation at late epochs make this behavior suspect. In particular, the non-thermal ionization from radioactive gamma rays becomes significant at low temperatures (Swartz 1991) and will keep the ejecta from ever going completely neutral. This may minimize or delay the putative third maximum. In addition, emission by forbidden transitions (not included here) may also become significant at these epochs. Meanwhile, most published SN Ia observations lack NIR data at times > 60 days after maximum.

6. DEPENDENCE ON PHYSICAL PARAMETERS

The above explanation of the NIR secondary maximum provides immediate insight into the dependence of the NIR light curves on the physical properties of the ejecta. This allows for simple explanations of the observed trends concerning the timing and prominence of the secondary maximum.

First, the rise to a secondary maximum occurs when the $2 \rightarrow 1$ ionization front first reaches the ejecta layers rich in iron group elements. Thus, the timing of the secondary maximum will depend on both the size of the iron core (or more precisely, its velocity extent) and the overall temperature scale of the ejecta. All other things being equal, SNe with larger iron cores can be expected to have earlier secondary maxima. Hotter SNe can be expected to have later ones.

Second, the luminosity of the secondary maximum depends fundamentally on the size and luminosity of the fluorescent shell formed when the $2 \rightarrow 1$ recombination wave has receded into the bulk of the iron core. All other things being equal, SNe Ia with larger iron cores can be expected to have a brighter secondary maximum.

Below we discuss these behaviors in the context of SN Ia ejecta properties. In particular, we consider the effects of the degree of mixing, the ^{56}Ni mass, the mass of electron capture elements,

the progenitor metallicity, and the mass of intermediate elements produced, demonstrating each of these with the models.

6.1. Mixing

The fiducial SN Ia model studied in § 5 was compositionally stratified, with iron group elements (primarily ^{56}Ni) concentrated in the central core. The mixing of ^{56}Ni outward into the region of IMEs effectively increases the velocity extent of the iron core. Naturally, we expect this to hasten the occurrence of the NIR secondary maximum.

We demonstrate this effect by comparing the NIR light curves of our fiducial model (mixing parameter $a_{\text{Ni}} = 0.2$) to one in which ^{56}Ni is more thoroughly mixed outwardly ($a_{\text{Ni}} = 0.5$). The result of the mixing (Fig. 9) is to advance the NIR secondary maximum by about 5 days and to decrease its contrast with the first maximum. In the I - and J -band light curves, the first and second maxima are blended, but still distinguishable. In the H - and K -band light curves the double-peaked structure is nearly lost entirely.

In Figure 9 we show also the light curves of a fully mixed model (i.e., the fiducial model with a completely homogenized compositional structure). In this case, the first and second maxima are indistinguishable in every band (except for perhaps a small inflection at day 35 in J). We conclude that the double-peaked structure observed in NIR light curves is a direct indication of the abundance stratification in SNe Ia, in particular, the concentration of iron-peak elements in the central regions. Thus, NIR observations should be useful in constraining the exact degree of mixing in SNe Ia.

6.2. Mass of ^{56}Ni

The mass of ^{56}Ni (M_{Ni}) powers the luminosity of SNe Ia and is the primary determinate of the peak brightness of the event. The M_{Ni} also affects, in part, the B -band light curve decline rate (or stretch) and is commonly identified as the fundamental parameter controlling the well-known width-luminosity relation.

In observations, the properties of the I -band secondary maximum are found to correlate with stretch (and hence peak luminosity), being more prominent and occurring later in the broader/brighter SNe Ia. The origin of these empirical relations can be addressed within the theoretical paradigm we have described. To demonstrate, we construct a series of models (based on the fiducial model) in which we vary M_{Ni} between 0.1 and $0.9 M_{\odot}$ in increments of $0.1 M_{\odot}$. The sum of M_{Ni} and the mass of IMEs is held fixed at $1.25 M_{\odot}$, such that all models have roughly equal kinetic energy. All other model parameters have been held fixed.

As in observations, the model secondary maxima are more pronounced in the higher M_{Ni} models, disappearing altogether for the lowest M_{Ni} models (Fig. 10). This is due primarily to the larger size of the iron core in higher M_{Ni} models, leading to a larger and more luminous fluorescent shell at the $2 \rightarrow 1$ ionization front. The observed behavior may therefore be taken as further evidence that more slowly declining SNe Ia have a larger production of iron group elements.

The M_{Ni} produces two opposing effects on the timing of the secondary maximum. A larger M_{Ni} leads to higher overall temperatures and thus a later development of the $2 \rightarrow 1$ recombination wave. This tends to delay the secondary maximum. However, a larger M_{Ni} also implies a larger iron core, which would tend to hasten the secondary maximum. From Figure 10, we see that the first of these effects dominates, at least for M_{Ni} in the range 0.1 – $0.8 M_{\odot}$. Thus, our models recover the observed timing

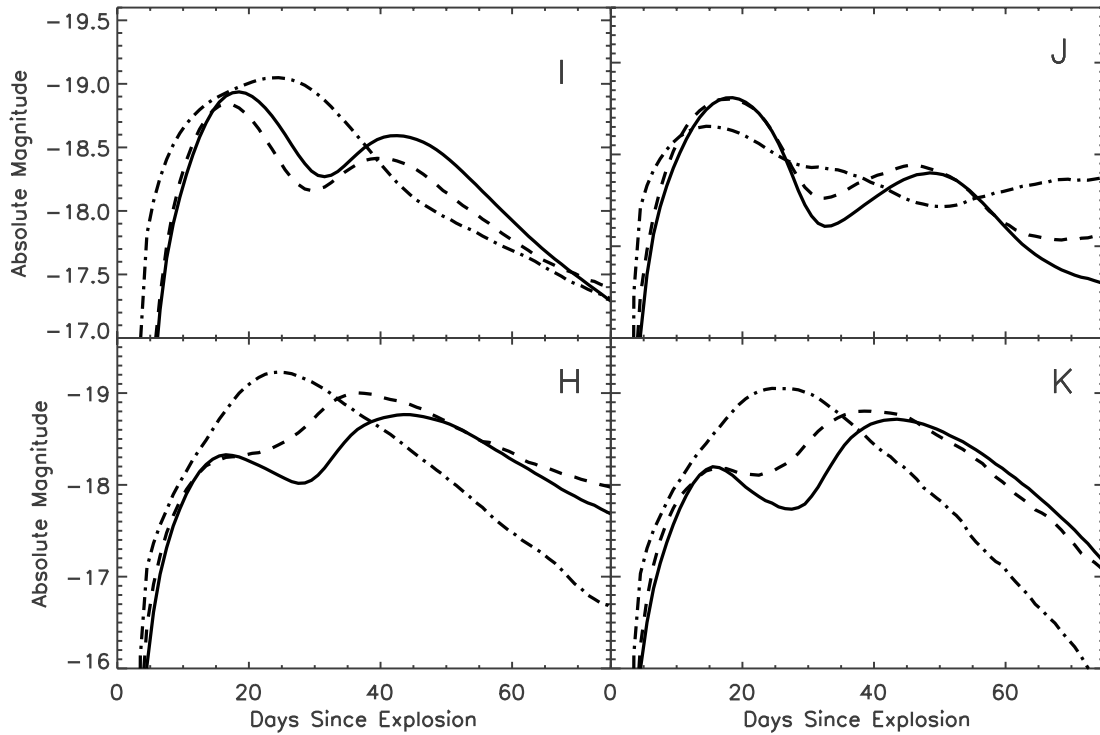


FIG. 9.—Effect of the outward mixing of ^{56}Ni on the NIR light curves. The figure compares the well-stratified fiducial model (mixing parameter $a_{\text{Ni}} = 0.2$; solid lines) to a model with enhanced ^{56}Ni mixing ($a_{\text{Ni}} = 0.6$; dashed lines) and a model with a completely homogenized composition structure (dot-dashed lines). [See the electronic edition of the Journal for a color version of this figure.]

trend, which should be interpreted as the physical correlation between the supernova's luminosity and its ionization state.

For the models with low M_{Ni} , the secondary maximum occurs at early times and begins merging with the initial maximum. In our most subluminal example ($M_{\text{Ni}} = 0.1 M_{\odot}$) the ejecta are so cool

that the $2 \rightarrow 1$ recombination wave reaches the iron core at $t_{\text{exp}} \approx 20$ days. For these objects, the secondary maximum is absent, or rather, it is coincident with the first.

For reference, Figure 11 quantifies the timing and prominence relations in the I and J bands. We note that the observed trends

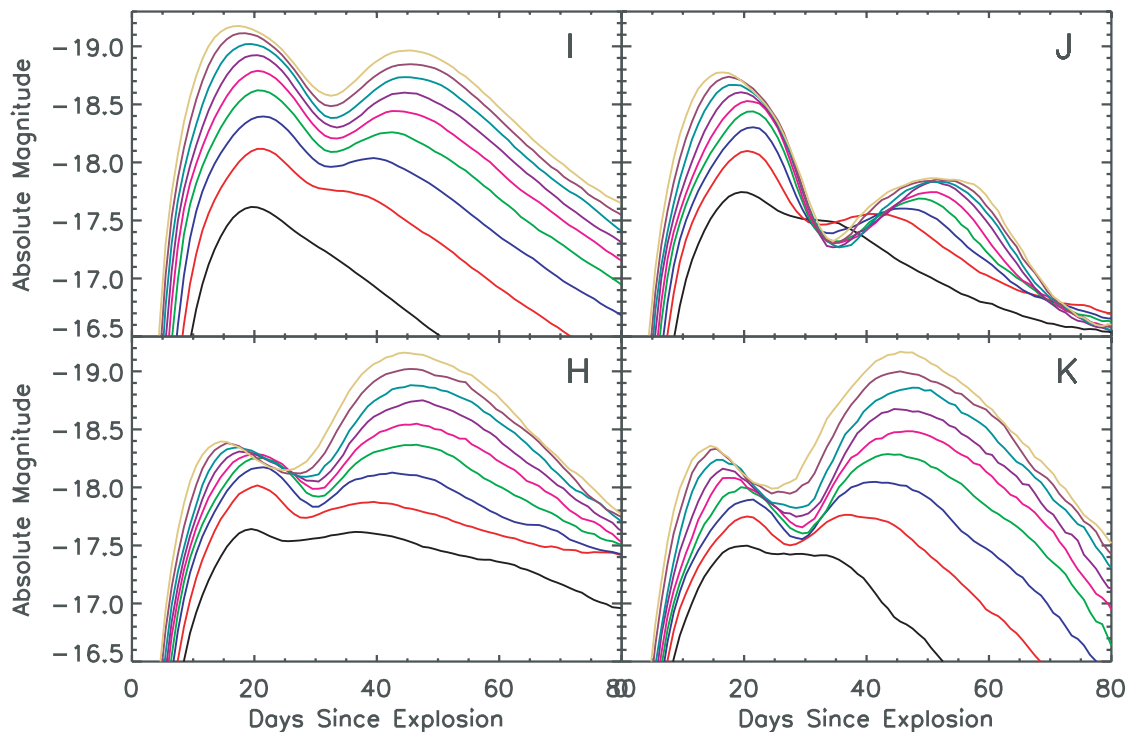


FIG. 10.—Effect of the mass of ^{56}Ni (M_{Ni}) on the NIR light curves. The model light curves demonstrate variations in M_{Ni} from 0.1 to $0.9 M_{\odot}$ in $0.1 M_{\odot}$ increments. The less luminous models are those with lower M_{Ni} .

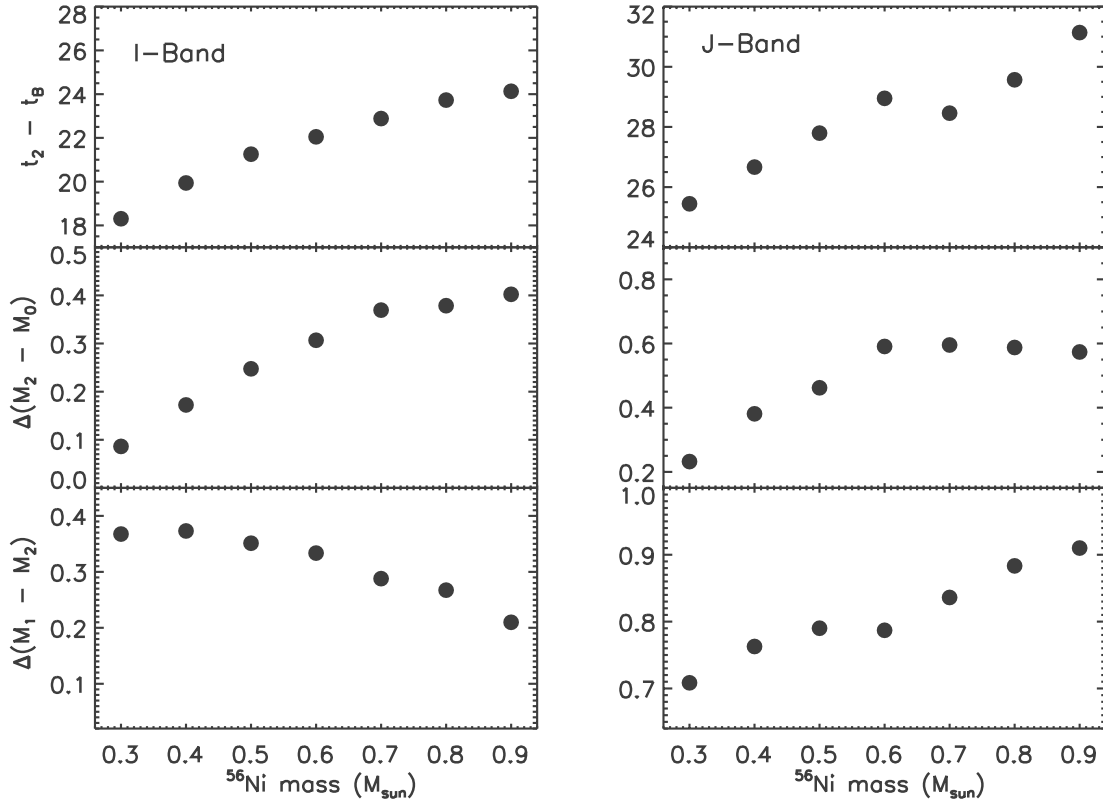


FIG. 11.—Prominence and timing of the secondary maximum vs. M_{Ni} for the models of Fig. 10 in the *I* band (left) and the *J* band (right). *Top*: Time (in days) of secondary maximum minus time of first maximum. *Middle*: Number of magnitudes by which the secondary maximum is brighter than the local minimum that precedes it. *Bottom*: Number of magnitudes by which the first maximum is brighter than the secondary maximum.

depend to some extent on how the quantities are empirically defined. In the *J* band, for example, the peak magnitude of the secondary maximum increases with M_{Ni} relative to the magnitude at the local minimum, but *decreases* relative to the first maximum. This reflects complexities glossed over in our discussion (such as the parameters affecting the initial maximum) and demonstrates the need to compare observations and models in a uniform way. Also keep in mind that additional parameters (described below) can also have profound effects on the secondary maximum and may play a role in these relations as well.

6.3. Electron Capture Elements and Progenitor Metallicity

In addition to ^{56}Ni , SNe Ia may synthesize substantial amounts of stable iron group elements, in particular ^{54}Fe and ^{58}Ni . Although this material does not contribute to the overall luminosity of the SN, it does modify the radial extent of the iron core. Thus, we anticipate it having important effects on the timing and prominence of the secondary maximum.

Stable iron group material can be produced by two distinct processes in SN Ia explosions: (1) In standard 1D explosion models, nuclear burning at the highest densities is subject to electron capture, leading to the synthesis of $0.5\text{--}2.0 M_{\odot}$ of neutronized stable iron group species at the very center of the ejecta (Nomoto et al. 1984; Thielemann et al. 1986). There is some observational evidence suggesting that such a pure stable iron center does exist in SNe Ia (Höflich et al. 2004). (2) While burning to nuclear statistical equilibrium produces primarily ^{56}Ni , some small fraction of stable iron group species may also be produced, depending on the metallicity of the progenitor white dwarf (Thielemann et al. 1986; Timmes et al. 2003). For solar metallicity, this fraction would be $\sim 5\%$, while for metallicity 3 times solar the fraction may be

as high as $\sim 25\%$. The stable iron group material arising from the progenitor metallicity would be evenly distributed in low abundance throughout the ^{56}Ni zone.

We demonstrate each of these effects in turn. First, we vary the mass of stable iron group species (M_{Fe}) produced by electron capture at the ejecta center. We explore values of M_{Fe} from 0 to $3.0 M_{\odot}$ while keeping fixed $M_{\text{Ni}} = 0.6 M_{\odot}$ and the total burned mass $M_{\text{Fe}} + M_{\text{Ni}} + M_{\text{IME}} = 1.25 M_{\odot}$. Figure 12 shows the resulting NIR light curves. Because the mass of ^{56}Ni is held fixed, the temperature and ionization evolution is very similar in all these models. However, in models with larger values of M_{Fe} (and hence larger iron cores) the $2 \rightarrow 1$ recombination wave encounters the layers of iron-rich material at relatively earlier times. The secondary maximum thus occurs as many as 10 days earlier in models with larger M_{Fe} . In addition, the peak magnitude of the secondary maximum increases with M_{Fe} , again due to the larger iron core size.

Pinto & Eastman (2000) have suggested that the stable iron group material at the ejecta center plays a fundamental role in producing the NIR secondary maximum. We note that this is not strictly the case, as a clear secondary maximum occurs even when no stable iron is included in the model.

One finds a similar dependence on the stable iron production due to progenitor metallicity. In Figure 13 we take the fiducial model and vary the abundance of stable ^{54}Fe throughout the ^{56}Ni zone from zero to 25%, corresponding to a metallicity variation of roughly zero to 3 times solar. The total mass in the ^{56}Ni zone is held fixed at $0.6 M_{\odot}$; i.e., in this construction stable iron is produced at the expense of ^{56}Ni . Thus, the higher metallicity model has lower bolometric luminosity, lower temperatures, and an earlier onset of the $2 \rightarrow 1$ recombination wave. The secondary

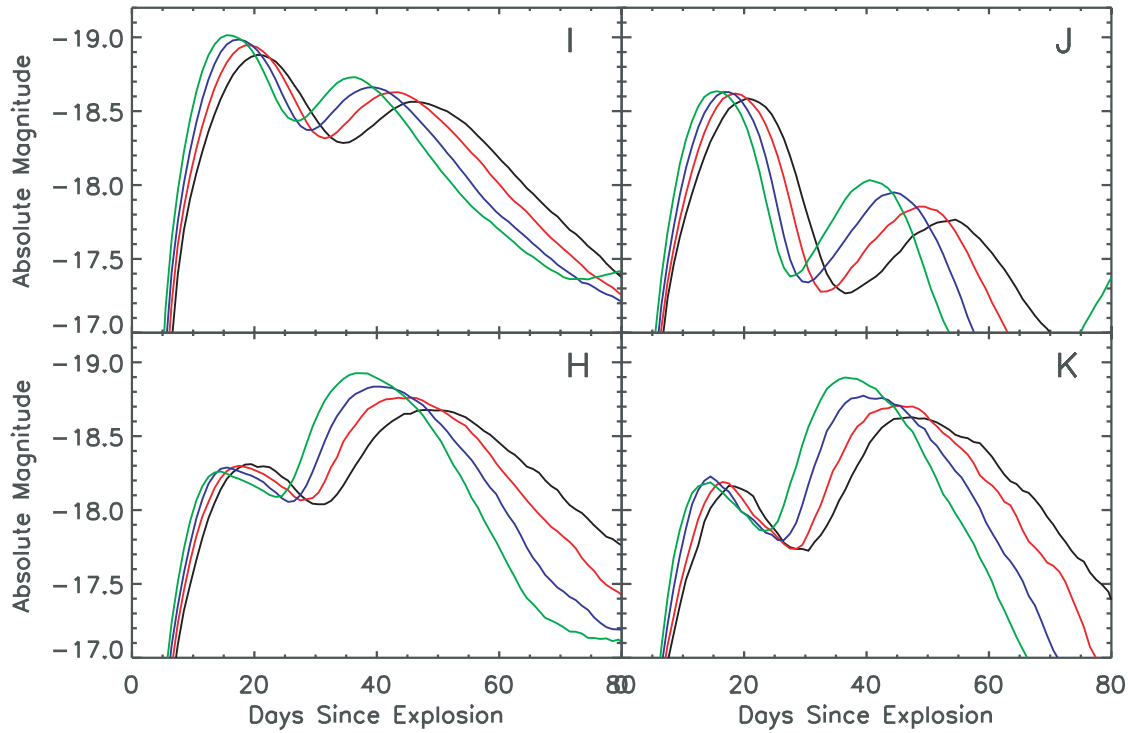


FIG. 12.—Effect of electron capture elements on the NIR light curves. The model light curves demonstrate variations in the mass of stable iron group elements (M_{Fe}) produced by electron capture at the ejecta center. The models are $M_{\text{Fe}} = 0.0 M_{\odot}$ (black line), $M_{\text{Fe}} = 0.1 M_{\odot}$ (red line), $M_{\text{Fe}} = 0.2 M_{\odot}$ (blue line), and $M_{\text{Fe}} = 0.3 M_{\odot}$ (green line).

maximum thus occurs about 7 days earlier in the higher metallicity model.

Because the size of the iron core remains fixed in the models of Figure 13, one expects the absolute luminosity of the secondary maximum to remain nearly constant. This is indeed the case in

the *I* and *J*-band light curves. Interestingly, however, the *H*- and *K*-band secondary maximum are slightly brighter in the low-metallicity models. This is due to the significantly larger emissivity of cobalt compared to iron at these wavelengths (see Fig. 3). Thus, the relative strength of the secondary maxima in different

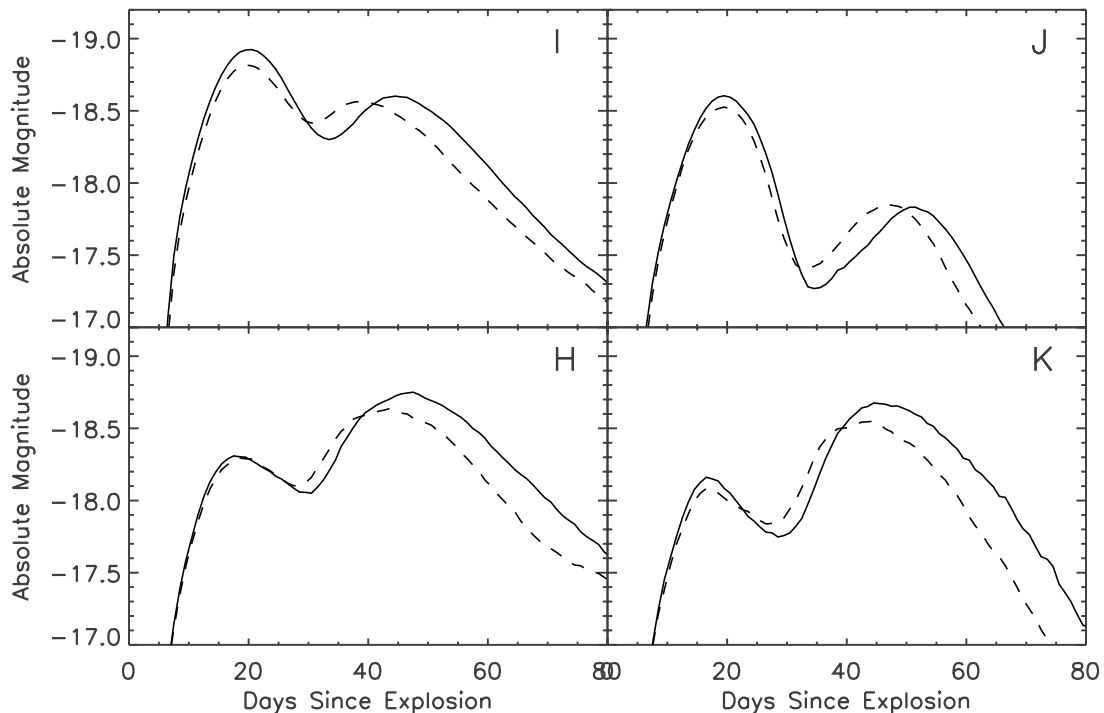


FIG. 13.—Effect of progenitor metallicity on the NIR light curves. The solid line shows the fiducial model with zero stable iron production in the ^{56}Ni zone (corresponding to near-zero metallicity). The dashed line shows the model with 25% stable iron production throughout the ^{56}Ni zone (corresponding to a metallicity near 3 times solar). [See the electronic edition of the *Journal* for a color version of this figure.]

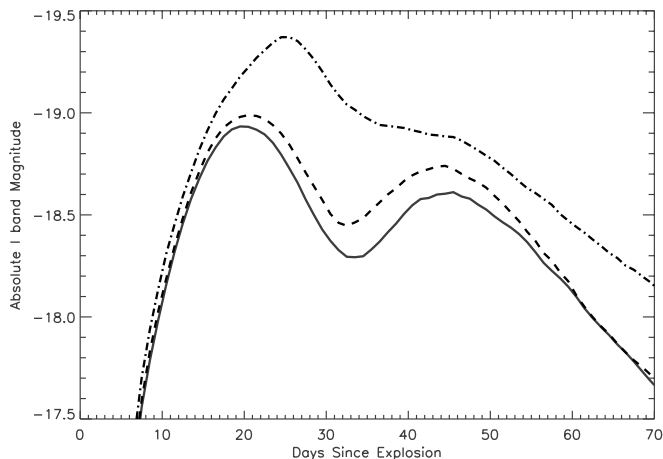


FIG. 14.—Effect of the Ca II IR triplet feature on the *I*-band light curve. For reference, the dashed line shows the fiducial model light curve when all calcium is removed. If the calcium lines are assumed to be pure scattering, the IR triplet feature leads to a modest decrease in the *I*-band magnitude (solid line). If the calcium lines are assumed to be purely absorbing, emission in the triplet feature increases the *I*-band magnitude significantly (dot-dashed line). [See the electronic edition of the *Journal* for a color version of this figure.]

NIR bands may turn out to be a useful measure of the ratio of cobalt to iron in the bulk ejecta and hence the progenitor metallicity.

Significantly, the effect of stable iron group elements on the NIR light curves is distinct from that of ^{56}Ni . The predicted correlation (i.e., earlier secondary maxima are as bright or brighter than later ones) conflicts with the primary observed trend. Variations in iron group elements are thus one potential source of deviation from the standard NIR light-curve behavior. This emphasizes the value of NIR observations in providing constraints of the progenitor metallicity and the early explosion processes.

6.4. Calcium Distribution and the IR Triplet Feature

On the whole, the distribution of IMEs in the ejecta has little direct effect on the NIR light curves. Emission from iron group lines dominates the continuum flux, and few individual IME line features are significant. The one exception is in the *I* band, where the prominent Ca II IR triplet feature (*gf*-weighted rest wavelength 8579 Å) can affect the photometry significantly. The triplet lines are intrinsically very strong and may remain optically thick far out in the low-density layers of ejecta, even when the calcium abundance is very low ($X_{\text{Ca}} \approx 0.01$).

Unfortunately, the net effect of the Ca II lines on the *I*-band light curve depends on the details of the radiative transfer, specifically the line source functions. Two limiting cases can be considered: (1) If the calcium lines are assumed to be pure scattering, flux is nearly conserved over the line profile; i.e., the absorption component of the P Cygni profile nearly cancels the emission component. In this case, the line feature should have only a minor effect on the broadband magnitude. (2) If, on the other hand, the calcium lines are assumed to be completely absorbing (as in pure LTE calculations), the net emission in the Ca II IR triplet feature can be considerable, because radiation absorbed in the blue part of the spectrum is allowed to reemerge in the triplet lines. In the models of this paper we have always assumed pure scattering calcium lines, for the reasons described below.

Figure 14 quantifies the net effect of calcium on the *I*-band light curve by comparing the fiducial model to a similar model in which all calcium has been removed. Under the pure scattering assumption, the Ca II triplet feature causes modest (~ 0.1 mag)

I-band differences. These arise for two reasons. First, because of blending with other lines, flux is not strictly conserved over the triplet line profile. Second, because the Bessell (1990) *I*-band filter profile cuts off near 8500 Å, the absorption and emission components of the triplet feature are not equally sampled. Thus, under pure scattering, the calcium feature serves to slightly *decrease* the *I*-band magnitude.

If, on the other hand, the calcium lines are assumed to be purely absorbing, net emission in the triplet features enhances the peak *I*-band magnitude by ~ 0.5 mag and delays the time of the peak by nearly 7 days. The secondary maximum is no longer distinct and prominent, and the model *I*-band light curve does not fit the observed light curve shape or colors. This result emphasizes that the *I*-band secondary maximum does not occur because of emission in the Ca II triplet feature, but rather *in spite* of it.

From an atomic physics perspective, the low collisional rates in the SN ejecta and the large oscillator strength of the Ca II triplet lines suggest that pure scattering is indeed the more plausible representation of the line source functions. This is supported by our light curve fits to the SN 2001el observations. To the extent that pure scattering does hold, the shape and peak brightness of the *I*-band light curves of SNe Ia will be generally insensitive (at the $\lesssim 0.1$ mag level) to the details of calcium production and distribution. This is an important condition for the robust application of *I*-band light curves to cosmology studies. One interesting exception is worth noting: if the calcium distribution deviates from spherical symmetry, flux scattered in the triple feature will be redistributed anisotropically along different viewing angles.

The results of this section require that a non-LTE treatment of the calcium level populations be included in the fully time-dependent multidimensional radiative transfer calculation. This solution is in fact readily incorporated into the Monte Carlo approach and will be included in the upcoming version of SEDONA. The common adoption of purely absorbing lines in previous LTE radiative transfer studies may be another reason why those calculations often encountered difficulty in fitting the *I*-band light curves of SNe Ia.

7. NEAR-IR SN Ia AS STANDARD CANDLES

The cosmological interest in NIR observations of SNe Ia stems from the small observed dispersion (~ 0.2 mag) in the peak *JHK*-band magnitudes. We explore this property here using the models discussed in § 6.2 (and shown in Fig. 10) for which the mass of ^{56}Ni is varied. We consider only those models with ^{56}Ni mass in the “normal” range, $0.4\text{--}0.9 M_{\odot}$.

Figure 15 shows the spread in model peak magnitude (measured at the first maximum) as a function of broadband filter. One notes a general decline in the dispersion toward the red. In the *B* band, the spread is roughly ± 0.5 mag, similar to the observed (uncorrected) dispersion (Hamuy et al. 1996a). This decreases to ± 0.4 mag in *V* and ± 0.3 mag in *R* and *I*. In the NIR the dispersion is more than a factor of 2 in magnitude smaller than the *B* band, being ~ 0.2 mag in *J* and *K* and ~ 0.1 mag in *H*. For the *H* and *K* bands, bear in mind the failure of the models to fix the observed first maximum, presumably an inadequacy of the atomic data. Nevertheless, this level of NIR dispersion is very similar to that inferred from observations (Meikle 2000).

In addition, the model peak NIR magnitudes show an impressive insensitivity to the other physical parameters explored in this paper. Significant variations in the progenitor metallicity, electron capture elements, and IME production all led only to small (~ 0.1 mag) variations in the absolute magnitude of the initial peak (Figs. 12, 13, and 14). The mixing of ^{56}Ni also caused only slight magnitude variations unless extreme levels of mixing

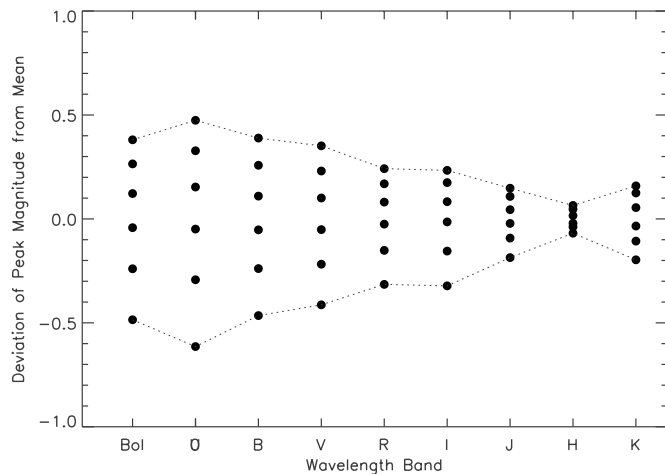


FIG. 15.—Dispersion in peak magnitude (measured at the first light curve maximum) as a function of wavelength band for the models of Fig. 10 with ^{56}Ni masses between 0.4 and $0.9 M_{\odot}$. [See the electronic edition of the *Journal* for a color version of this figure.]

were considered (Fig. 9). These results further testify to the robustness of SN Ia NIR light curves as standard candles.

Our model light curves may also suggest further refinements to cosmology studies in the NIR. The J -band light curves, for example, show almost *zero* intrinsic dispersion at the local minimum occurring between the first and secondary maximum (about 15 days after B -band maximum; see Fig. 10). Even when the subluminal models are considered, the magnitude variations at this epoch are small. It would be interesting to check whether observed SNe Ia exhibit a similar behavior. As it turns out, Meikle (2000) chose to study the J -band magnitudes of SNe Ia measured 14 days after B -band maximum (as derived from fits to the Elias et al. (1985) templates). He found that the dispersion in $M_{14}(J)$ was small, although not necessarily minimal.

The low peak magnitude dispersion in the NIR follows from the dependence of the model colors on the bolometric luminosity. The dimmer SNe also have lower temperatures and radiate a greater percentage of the energy at redder wavelengths. This acts as a regulating mechanism that maintains a nearly constant peak magnitude in the NIR bands, regardless of the ^{56}Ni mass. On the other hand, the dispersion in ultraviolet and U -band magnitudes is reciprocally intensified, exceeding that of the bolometric light curves.

8. DISCUSSION AND CONCLUSION

We have modeled the far-red and NIR light curves of SNe Ia and given a detailed explanation of the characteristic secondary maximum. Our synthetic model light curves were calculated using parameterized 1D ejecta configurations and the time-dependent multigroup radiative transfer code SEDONA. The model light curves displayed distinct and conspicuous secondary maxima and provided favorable fits to the NIR observations of the normal Type Ia SN 2001el. By varying the mass of ^{56}Ni , the models also reproduced the observed trend that brighter SNe Ia have later and more prominent secondary maxima.

We trace the origin of the secondary maximum directly to the ionization evolution of iron group elements in the ejecta. Specifically, the NIR emissivity of iron/cobalt gas peaks sharply at a temperature $T_{21} \approx 7000$ K, marking the transition between the singly and doubly ionized states. The recombination of iron-rich gas from $2 \rightarrow 1$ thus leads to enhanced redistribution of radiation from blue to NIR. Interestingly, as the supernova cools, the global

ionization evolution takes the form of a $2 \rightarrow 1$ “recombination wave” gradually receding deeper into the ejecta. The onset and propagation of this wave through the iron-rich layers marks the rise and fall the secondary maximum. Because the ejecta are transparent at longer wavelengths during these epochs, the NIR observations allow us to watch directly as the recombination wave scans through progressively deeper layers of ejecta.

While the models considered in this paper captured the essential aspects of SN Ia NIR light curves, they also highlighted several outstanding issues for the radiative transfer calculations. First, the use of a complete and accurate atomic line list proved critical in modeling the NIR bands. Further improvement of the currently available atomic data is likely needed to accurately model the H - and K -band light curves. Second, nonthermal ionization effects from radioactive gamma rays become significant for $t_{\text{exp}} \gtrsim 70$ days, when LTE predicts neutrality, and thus likely have a dramatic impact on the NIR light curves at these late epochs. Third, a proper treatment of Ca II IR triplet line source function is crucial in synthesizing accurate I -band model light curves, as the assumption of purely absorbing lines leads to unrealistic results. Future advances in the SEDONA code will permit more detailed studies of these and other important effects. However, one does not expect the technical developments to change the general NIR light curve trends and dependencies explained in this paper.

In this paper, we studied the dependence of the NIR light curves on a number of important physical parameters, which highlighted the many ways in which NIR light curves offer valuable diagnostics of the ejecta properties and powerful constraints on explosion models. First, the double-peaked morphology of the NIR light curves can be taken as a direct consequence of the abundance stratification in SNe Ia, in particular, the concentration of iron group elements in the central regions. This confirms previous inferences based on postmaximum and nebular spectra (e.g., Branch et al. 1985; Höflich et al. 2002; Kozma et al. 2005). Abundance stratification is generic to certain classes of explosion models, for example, the delayed-detonation models (Khokhlov 1991) and the detonation-from-failed-detonation models (Plewa et al. 2004). In contrast, models characterized by large-scale mixing, such as published three-dimensional deflagration models (Gamezo et al. 2003; Reinecke et al. 2002), are likely inconsistent with the double-peaked behavior in the NIR light curves. Further NIR observations, coupled with the transfer models, should be useful in constraining the exact degree of ^{56}Ni mixing in SNe Ia and thus in testing current and future explosion paradigms.

Second, the luminosity of the secondary maximum provides a measure of the amount of iron group elements (both stable and radioactive) synthesized in the explosion. The observed correlation between the B -band decline rate and the luminosity of the secondary maximum provides strong evidence that slower declining SNe Ia have (on average) a larger production of iron group elements. This conclusion coincides with several other inferences to the same (Contardo et al. 2000; Mazzali et al. 1998; Stritzinger et al. 2006).

Third, the NIR secondary maximum is sensitive to the amount of stable iron group elements produced in the explosion and hence the progenitor metallicity. Timmes et al. (2003) has suggested that metallicity variations may lead to 25% variations in ^{56}Ni . We find that the NIR signature of this variation is distinct from that of varying ^{56}Ni independently. Our predicted correlation arising from metallicity variations is that the earlier secondary maxima will be as bright as or brighter than the later ones. This conflicts with the primary observed trend and suggests that the metallicity is likely a subdominant cause of SN Ia luminosity variations. This

signature widens the possibility of using an observational sample of NIR light curves to constrain metallicity variations among different progenitor populations.

Fourth, the timing of the secondary maximum is a direct probe of the temperature and ionization evolution in the ejecta and hence a useful tool in interpreting observations. As it turns out, the ionization evolution is of crucial importance to the optical light curve decline rate as well. The $2 \rightarrow 1$ recombination of iron group elements contributes significantly to blanketing in the *B* and *V* bands, due to the development of blends of strong Fe II and Co V lines in the optical part of the spectrum. In this context, NIR observations may also be especially useful in diagnosing peculiar objects. For example, the paradoxical SN 2002cx was ~ 2 mag subluminous, but had a peculiar spectrum characteristic of “hot” iron-rich ejecta (Li et al. 2003). NIR observations would complement those spectroscopic analyses by providing independent measures of the temperature scale, ionization evolution, iron core size, and mixing.

Finally, we reiterate the cosmological utility of the NIR light curves of SNe Ia. In our light curve models, the dispersion in NIR peak magnitudes is found to be small ($\lesssim 0.2$ mag), even when the physical properties of the ejecta are varied widely. At certain epochs (e.g., the *J*-band local minimum occurring near day 15 after *B*-band maximum) the predicted dispersion is even smaller. Our models thus further testify to the robustness of SN Ia NIR light curves as standard candles.

Perhaps more importantly, the NIR observations provide deep and readily interpreted diagnostics of the physical conditions in

the SN Ia ejecta and therefore offer an opportunity for controlling potential systematic errors in the cosmology studies. We have shown that the physical parameters affecting the NIR secondary maximum are also those that may modulate the optical peak brightness and decline rate of SNe Ia. Thus, the NIR light curves are one of the most promising places to search for empirical secondary parameters related to deviations from the standard width-luminosity relation.

In this context, the NIR observations strike a nice balance in their level of information content. Given the double-peaked morphology, the NIR light curves carry considerably more information than do the single-peaked optical band observations; at the same time, they remain simple enough to submit much more readily to statistical analysis than do the complex spectral time series. For all these reasons, a sizable sample of observed NIR light curves would be a remarkably powerful tool in constraining the possible evolution or progenitor drift of SNe Ia arising in differing stellar populations. This potential should be exploited further with expanded observational programs and concerted theoretical efforts.

The author thanks Kevin Krisciunas and Peter Meike for helpful comments and suggestions. This research used resources of the National Energy Research Scientific Computing Center, which is supported by the Office of Science of the US Department of Energy under contract DE-AC03-76SF00098.

REFERENCES

- Arnett, W. D. 1982, *ApJ*, 253, 785
 Baron, E., Hauschildt, P. H., Nugent, P., & Branch, D. 1996, *MNRAS*, 283, 297
 Bessell, M. S. 1990, *PASP*, 102, 1181
 Blinnikov, S., & Sorokina, E. 2004, *Ap&SS*, 290, 13
 Bowers, E. J. C., Meikle, W. P. S., Geballe, T. R., Walton, N. A., Pinto, P. A., Dhillon, V. S., Howell, S. B., & Harrop-Allin, M. K. 1997, *MNRAS*, 290, 663
 Branch, D., Doggett, J. B., Nomoto, K., & Thielemann, F.-K. 1985, *ApJ*, 294, 619
 Candia, P., et al. 2003, *PASP*, 115, 277
 Contardo, G., Leibundgut, B., & Vacca, W. D. 2000, *A&A*, 359, 876
 Eastman, R. G., & Pinto, P. A. 1993, *ApJ*, 412, 731
 Elias, J. H., Frogel, J. A., Hackwell, J. A., & Persson, S. E. 1981, *ApJ*, 251, L13
 Elias, J. H., Matthews, K., Neugebauer, G., & Persson, S. E. 1985, *ApJ*, 296, 379
 Gamezo, V. N., Khokhlov, A. M., Oran, E. S., Chtchelkanova, A. Y., & Rosenberg, R. O. 2003, *Science*, 299, 77
 Hamuy, M., Phillips, M. M., Suntzeff, N. B., Schommer, R. A., Maza, J., & Aviles, R. 1996a, *AJ*, 112, 2398
 Hamuy, M., Phillips, M. M., Suntzeff, N. B., Schommer, R. A., Maza, J., Smith, R. C., Lira, P., & Aviles, R. 1996b, *AJ*, 112, 2438
 Hernandez, M., et al. 2000, *MNRAS*, 319, 223
 Höflich, P. 1995, *ApJ*, 443, 89
 Höflich, P., Gerardy, C. L., Fesen, R. A., & Sakai, S. 2002, *ApJ*, 568, 791
 Höflich, P., Gerardy, C. L., Nomoto, K., Motohara, K., Fesen, R. A., Maeda, K., Ohkubo, T., & Tominaga, N. 2004, *ApJ*, 617, 1258
 Höflich, P., & Khokhlov, A. 1996, *ApJ*, 457, 500
 Höflich, P., Khokhlov, A. M., & Wheeler, J. C. 1995, *ApJ*, 444, 831
 Karp, A. H., Lasher, G., Chan, K. L., & Salpeter, E. E. 1977, *ApJ*, 214, 161
 Kasen, D., et al. 2003, *ApJ*, 593, 788
 ———. 2006, *ApJ*, submitted
 Khokhlov, A. 1991, *A&A*, 245, 114
 Kirshner, R. P., Willner, S. P., Becklin, E. E., Neugebauer, G., & Oke, J. B. 1973, *ApJ*, 180, L97
 Kozma, C., Fransson, C., Hillebrandt, W., Travaglio, C., Sollerman, J., Reinecke, M., Röpke, F. K., & Spyromilio, J. 2005, *A&A*, 437, 983
 Krisciunas, K., Phillips, M. M., & Suntzeff, N. B. 2004a, *ApJ*, 602, L81
 Krisciunas, K., et al. 2001, *AJ*, 122, 1616
 ———. 2003, *AJ*, 125, 166
 ———. 2004b, *AJ*, 127, 1664
 ———. 2004c, *AJ*, 128, 3034
 Kurucz, R. 1993, CD-ROM 1, Atomic Data for Opacity Calculations (Cambridge: SAO)
 Li, W., et al. 2003, *PASP*, 115, 453
 Marion, G. H., Höflich, P., Vacca, W. D., & Wheeler, J. C. 2003, *ApJ*, 591, 316
 Mazzali, P. A., Cappellaro, E., Danziger, I. J., Turatto, M., & Benetti, S. 1998, *ApJ*, 499, L49
 Mazzali, P. A., & Lucy, L. B. 1993, *A&A*, 279, 447
 Meikle, W. P. S. 2000, *MNRAS*, 314, 782
 Meikle, W. P. S., et al. 1996, *MNRAS*, 281, 263
 Mihalas, D. 1978, *Stellar Atmospheres* (2nd ed.; San Francisco: Freeman)
 Nobili, S., et al. 2005, *A&A*, 437, 789
 Nomoto, K., Thielemann, F., & Yokoi, K. 1984, *ApJ*, 286, 644
 Persson, S. E., Murphy, D. C., Krzeminski, W., Roth, M., & Rieke, M. J. 1998, *AJ*, 116, 2475
 Phillips, M. M., Lira, P., Suntzeff, N. B., Schommer, R. A., Hamuy, M., & Maza, J. 1999, *AJ*, 118, 1766
 Pinto, P. A., & Eastman, R. G. 2000, *ApJ*, 530, 757
 Plewa, T., Calder, A. C., & Lamb, D. Q. 2004, *ApJ*, 612, L37
 Reinecke, M., Hillebrandt, W., & Niemeyer, J. C. 2002, *A&A*, 391, 1167
 Rudy, R. J., Lynch, D. K., Mazuk, S., Venturini, C. C., Puetter, R. C., & Höflich, P. 2002, *ApJ*, 565, 413
 Stritzinger, M., Leibundgut, B., Walch, S., & Contardo, G. 2006, *A&A*, 450, 241
 Swartz, D. A. 1991, *ApJ*, 373, 604
 Thielemann, F.-K., Nomoto, K., & Yokoi, K. 1986, *A&A*, 158, 17
 Timmes, F. X., Brown, E. F., & Truran, J. W. 2003, *ApJ*, 590, L83
 Valentini, G., et al. 2003, *ApJ*, 595, 779
 Wang, L., et al. 2003, *ApJ*, 591, 1110
 Wheeler, J. C., Höflich, P., Harkness, R. P., & Spyromilio, J. 1998, *ApJ*, 496, 908